A perturbation analysis approach for studying the effect of swelling kinetics on instabilities in hydrogel plates

Arne Ilseng
Biomechanics
Department of Structural Engineering
NTNU, Norwegian University of Science and Technology
7491 Trondheim, Norway
Email: arne.ilseng@ntnu.no

Bjørn H. Skallerud
Biomechanics
Department of Structural Engineering
NTNU, Norwegian University of Science and Technology
7491 Trondheim, Norway

Bjørn T. Stokke
Biophysics and Medical Technology
Department of Physics
NTNU, Norwegian University of Science and Technology
7491 Trondheim, Norway

Victorien Prot
Biomechanics
Department of Structural Engineering
NTNU, Norwegian University of Science and Technology
7491 Trondheim, Norway

The onset of surface instability during diffusion-driven swelling of hydrogels depends on the kinetics of the swelling process. Here, we outline a perturbation analysis framework using a finite difference approach for calculating the stability limit of swelling hydrogel plates with graded material properties accounting for kinetic effects. The framework is implemented as a Python routine which is made freely available. Results obtained for bilayered hydrogel plates illustrate that onset of instability occurs earlier in time and at a lower global swelling ratio when kinetics is accounted for compared to the homogeneous swelling case. This work presents an accessible calculation tool for stability analysis of swelling gels, providing input for the design of novel hydrogel systems.

1 Introduction

Hydrogels are polymeric networks that swell in an aqueous solution through the diffusion of water. As these materials can be tuned to change their level of swelling as a response to characteristics of the surrounding solution (e.g. pH, temperature, salinity) they hold great potential for emerging applications like drug delivery systems [1–3], biological sensors [4,5], and responsive surfaces [6]. An intriguing feature of hydrogel materials is the possible occurrence of geometrical surface instabilities as a response to compressive stresses in the gel [7–10]. Swelling-induced compressive stresses can arise due to geometrical confinements [7], the transient nature of the diffusion process [11], or graded material properties [9]. Where graded material properties can be caused by a continuous variation in cross-linking den-

sity through the thickness of the gel [9, 12] or layering of the material [13–15]. The successful design of hydrogel systems relies on predictive methods for the stability of swelling gels providing sound stability diagrams. Previous computational studies on the instability of gels have made use of two main methods, finite element (FE) simulations [16–21] or perturbation analysis (PA) [22–27].

FE simulations have successfully been applied to study geometrical instability of transiently swelling gels in a few recent studies [19–21]. This method excels in its applicability to general geometries and loading conditions, and use of the method has demonstrated that the swelling kinetics can alter both the level of swelling and the wavelength of the surface pattern at the onset of instability. In particular, soft bilayered gels with a low stiffness ratio (i.e. the stiffness of the upper layer relative to the lower layer) have been shown to change their instability mode from a global long-wavelength wrinkling pattern to localized creasing as the speed of the swelling process is reduced [20, 21]. Nevertheless, the application of FE simulations of swelling gels in the design of new hydrogel systems can be limited by its requirements of advanced software, highly skilled analysts, and computational resources. Further, for simulations where localized creasing defines the initial instability mode of the gel, mesh dependence hinders accurate predictions for the level of swelling at the onset of instability [17].

The PA methodology excels in computation efficiency and availability, as it with relative ease can be implemented in an open-source programming language like Python. The PA framework is based on Biot's linear perturbation analysis of compressed elastomers [28] and was formulated for swelling gel plates with homogeneous material properties by Kang and Huang [22]. Wu *et al.* further extended the method to account for plates with bilayered material properties [25] and, using a subspace and a finite difference method, to gels with an arbitrary gradient in the material properties [27]. However, previous studies using PA for swelling gels have assumed a homogeneous chemical potential through the gel, meaning that the swelling kinetics of the problem has not been considered.

This work expands the PA methodology to account for the kinetics of the swelling process, to obtain a simple, available, and accurate computational approach to predict the stability of swelling hydrogels. The presented work improves on previously published studies in two main ways. i) We include gradients in the chemical potential of the gel in the PA method, hence accounting for the kinetics of diffusive swelling. ii) We make use of a non-uniform node distribution in the finite difference solution of the eigenvalue problem to significantly improve the computational efficiency. Further, the implementation of the framework described here is made freely available [29].

The presented method is used to study the instability of bilayered plates at the extremes of fast and slow diffusion. Hence, the stability plots obtained for slow diffusion adds new results compared to previous studies. Further, the proposed method sheds light on the competition between short- and long-wavelength instability modes for soft gels under slow diffusion.

The article is organized as follows: In the following section, we introduce the geometry and general characteristics of the studied problem. In Section 3, we outline the perturbation analysis method using a finite difference approach with a non-uniform node spacing and discuss its implementation in Python. Section 4 presents a demonstration of the proposed framework giving results for a bilayered structure. In the end, Section 5 draws the main conclusions from the study.

2 Problem definition

Consider an infinitely wide 2D plate of a hydrogel material having a height H at reference time t_0. The plate is represented in the reference coordinate system $\mathbf{X}$, as schematically shown in Fig. 1a. At its bottom ($X_2 = 0$), the gel is fixed to a rigid substrate providing an in-plane constraint. The upper surface ($X_2 = H$) can swell or shrink freely in the out-of-plane direction. The node numbering indicated in Fig. 1a will come to use in Section 3.4 and beyond. For further calculations, we introduce the normalized coordinate

$$\bar{X}_2 = X_2/H \tag{1}$$

We consider the gel to be in chemical equilibrium with its surroundings at t_0, meaning that it has a homogeneous normalized chemical potential $\bar{\mu}_0$. Then, assume that from time t_0 to t_1 the normalized chemical potential of the solvent change linearly from $\bar{\mu}_0$ to $\bar{\mu}_1$ with the upper surface of the gel being in equilibrium with the solvent. This will cause a gradient of the chemical potential through the thickness of the gel, which drives the diffusion of water into the plate. This diffusion of water causes swelling of the gel, giving it a new height h, as shown in Fig. 1b which represents the gel in the current coordinate system $\mathbf{x}$ (the surface perturbation in the figure will be further discussed in Section 3.3). The kinetics of the swelling process will depend on the initial height H, the time of the chemical potential increase $t_r = t_1 - t_0$, and the apparent diffusion coefficient of the solvent molecules D (having dimensions of m^2/s).

To relate the three relevant parameters we define the dimensionless ramping time

$$\bar{t}_r = t_r/\tau \tag{2}$$

where the characteristic swelling time τ is defined as $\tau = H^2/D$. The swelling kinetics of an arbitrary gel will then be within the limits of $\bar{t}_r = \infty$ and $\bar{t}_r = 0$. First, if $\bar{t}_r = \infty$ the whole gel will have time to equilibrate for all values of the chemical potential, hence, there will be a homogeneous potential through the thickness of the gel. Second, if $\bar{t}_r = 0$ we have an abrupt change in the boundary condition, and there will be an inhomogeneous chemical potential through the gel. Figure 2 illustrates the difference between the two limiting cases, showing the chemical potential through the

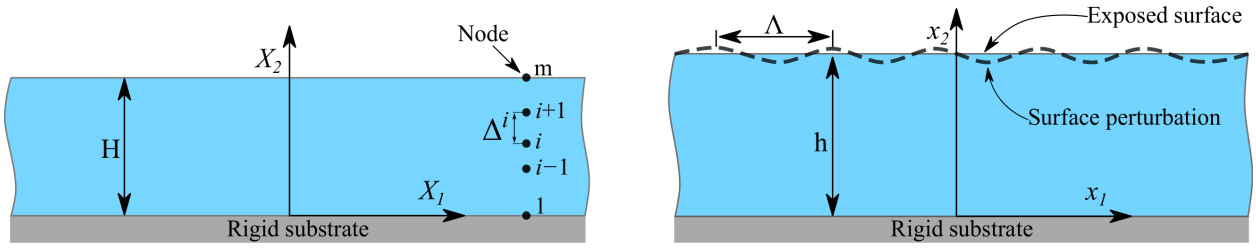

Fig. 1: Sketch of an infinitely wide hydrogel plate in *(a)* the reference configuration and *(b)* a swollen configuration with the dotted line indicating a perturbation of wavelength Λ. The lower boundary of the gel is attached to a rigid substrate while the upper surface is exposed to a solvent.

thickness of the gel at various time steps for $\bar{t}_r = \infty$ (Fig. 2a) and $\bar{t}_r = 0$ (Fig. 2b) given the chemical potential values $\bar{\mu}_0 = -2$ and $\bar{\mu}_1 = 0$ (the method for calculating the potential profiles and the values chosen for $\bar{\mu}_0$ and $\bar{\mu}_1$ are discussed further in Section 3.2). Note that the time t (being zero at t_0) is normalized by the ramping time t_r for the case of $\bar{t}_r = \infty$ and the characteristic swelling time τ for $\bar{t}_r = 0$.

We emphasize that the diffusion coefficient D is given by the hydrogel and solvent combination and typically lies in the range of $10^{-9} - 10^{-10}$ m^2/s [30]. Hence, for a given gel and solvent type the value of $\bar{t}_r$ can be changed by altering the ramping time of the chemical potential t_r or the initial gel height H. In the following, we will develop a methodology to calculate the stability of swelling gels for the limiting cases of $\bar{t}_r = \infty$ and $\bar{t}_r = 0$.

3 Methods

3.1 Constitutive formulation

To develop a perturbation analysis framework for swelling hydrogel plates, we first need a constitutive description of the process of confined swelling. The constitutive modeling of hydrogel behavior applied herein is based on the work by Hong *et al.* [31, 32]. The free-energy function for the hydrogel is assumed to originate from the stretching of the polymer network and the mixing of the polymer and the solvent molecules, and the two contributions add up to [33–35]

$$W(\mathbf{F},C) = \frac{1}{2}NkT\left[F_{iK}F_{iK} - 3 - 2\ln(\det\mathbf{F})\right] + \frac{kT}{v}\left[vC\ln\left(\frac{vC}{1+vC}\right) + \frac{\chi vC}{1+vC}\right] \tag{3}$$

where N is the number of polymeric chains per reference volume, kT is the temperature in the unit of energy, $\mathbf{F}$ is the deformation gradient tensor, v is the volume per solvent molecule, C is the nominal concentration of solvent molecules, and χ is the Flory-Huggins parameter. By assuming that both the polymer network and the solvent molecules retain their volumes through the swelling process, we find that the volume increase of the gel relies on an increase in the number of solvent molecules inside the gel, hence we can write

$$J = \det\mathbf{F} = 1 + vC \tag{4}$$

where J denotes the volume ratio of the gel. Through a Legendre transformation, we introduce a new potential $\hat{W}$ to ensure the deformation gradient $\mathbf{F}$ and the chemical potential μ to be the two independent variables of the model

$$\hat{W}(\mathbf{F},\mu) = W(\mathbf{F},C) - \frac{\mu}{v}(J-1) \tag{5}$$

The nominal stress components in the gel can then be found through

$$s_{iK} = \frac{\partial\hat{W}(\mathbf{F},\mu)}{\partial F_{iK}} = NkT\Big(F_{iK} - H_{iK} + \frac{1}{Nv}\left[J\ln\left(1-\frac{1}{J}\right) + 1 + \frac{\chi}{J} - \frac{\mu}{kT}J\right]H_{iK}\Big) \tag{6}$$

where $\mathbf{H} = \mathbf{F}^{-T}$. For the problem presented in Fig. 1, the plate is under constrained swelling, with the deformation gradient having the non-zero components $F_{11} = F_{33} = 1$ and $F_{22} = \lambda$, resulting in $J = \lambda$. The nominal out-of-plane stress component can then be written as

$$s_{22} = NkT\left[\lambda - \frac{1}{\lambda} + \frac{1}{Nv}\left(\ln\left(1-\frac{1}{\lambda}\right) + \frac{1}{\lambda} + \frac{\chi}{\lambda^2} - \bar{\mu}\right)\right] \tag{7}$$

where we have introduced the normalized chemical potential as $\bar{\mu} = \mu/kT$. If the gel is traction free at its upper surface, static equilibrium gives $s_{22} = 0$ and we get a non-linear relation between the swelling ratio and the chemical potential

$$Nv\left(\lambda - \frac{1}{\lambda}\right) + \ln\left(1-\frac{1}{\lambda}\right) + \frac{1}{\lambda} + \frac{\chi}{\lambda^2} = \bar{\mu} \tag{8}$$

The methodology for calculating the chemical profiles through time for $\bar{t}_r = \infty$ and $\bar{t}_r = 0$, as illustrated in Fig. 2, is the focus of the following section.

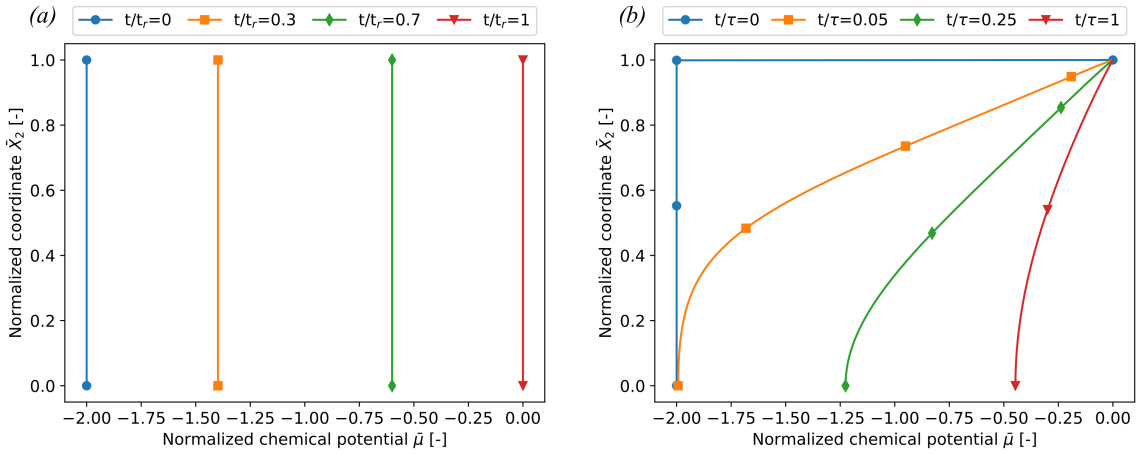

Fig. 2: The profile of the normalized chemical potential through the thickness of the gel at various times for the limiting cases *(a)* $\bar{t}_r = \infty$ and *(b)* $\bar{t}_r = 0$ (profiles obtained using the method outlined in Section 3.2). Note that the time step t is normalized by the ramping time t_r in *(a)* and by the characteristic swelling time τ in *(b)*.

3.2 Chemical potential profiles

For $\bar{t}_r = \infty$, the chemical potential through the thickness of the plate is simply assumed to be homogeneous at all times. The chemical potential is set to increase from $\bar{\mu}_0 = -2$ to $\bar{\mu}_1 = 0$, where $\bar{\mu}_0 = -2$ corresponds to an out-of-plane swelling of $\lambda \approx 1.04$ (with the exact value depending on the gel parameters Nv and χ).

For $\bar{t}_r = 0$, on the other hand, the profile of the chemical potential through the thickness of the plate must be calculated as a function of time for each set of material parameters (Nv and χ). From our previous FE simulations [21] we find that the flow of chemical potential is one dimensional up until the onset of instability. Hence, for the present study (which scope is limited to predictions of the onset of instability) we consider the flow of solvent only in the direction of the thickness of the gel and adopt the modeling procedure outlined by Hong *et al.* [31] and Bouklas and Huang [36]. Note that for studies of the post-buckling regime a multidimensional flow should be accounted for.

As the material properties are defined in the reference configuration, all equations are related to the normalized through-thickness coordinate $\bar{X}_2$. Further, as the dry state of the gel yields a singular set of equations, we assume that the plate initially is in an equilibrium state with a homogeneous normalized chemical potential of $\bar{\mu}_0$, and an isotropic deformation gradient $\mathbf{F}_0 = \lambda_0 \mathbf{I}$. From this initial state, the plate is confined from in-plane expansion but can still freely swell out-of-plane. The chemical potential is then abruptly changed to $\bar{\mu}_1 = 0$ at the upper surface (i.e. $\bar{t}_r = 0$) and the gel gradually expands in the X_2-direction giving a deformation gradient with the non-zero elements $F_{11} = F_{33} = \lambda_0$ and $F_{22} = \lambda\lambda_0$ where $\lambda = \lambda(\bar{X}_2, t)$. The swelling ratio of the gel can then be expressed as $J = \lambda_0^3 \lambda$.

It should be noted that the gradient in chemical potential through the thickness of a gel at a given time, and hence the stability limits obtained, would depend on the value of the homogeneous chemical potential $\bar{\mu}_0$. In this work, we set $\bar{\mu}_0 = -2$ to obtain an equilibrium state close to the dry state of the gel, with $\lambda_0 \approx 1.01$ (the exact value depending on the gel parameters Nv and χ).

A kinetic law for the gel can be written as

$$J_K = -M_{KL} \frac{\partial \mu}{\partial X_L} \tag{9}$$

where $\mathbf{J}(\mathbf{X}, t)$ is the nominal flux vector for the solvent molecules (not to be mixed with the volume ratio J), while the mobility tensor $\mathbf{M}$ is symmetric and positive-definite. The diffusion coefficient of the solvent molecules D is taken as isotropic and independent of the deformation gradient $\mathbf{F}$ and the concentration of solvent molecules C. It can be shown that the mobility tensor can be written as [21]

$$M_{KL} = \frac{D}{vkT} H_{iK} H_{iL} (\det \mathbf{F} - 1) \tag{10}$$

From the condition of molecular incompressibility (Eqn. (4)), we can express the nominal concentration of solvent molecules as

$$C(\bar{X}_2, t) = \frac{1}{v}(J - 1) = \frac{1}{v}\left(\lambda_0^3 \lambda - 1\right) \tag{11}$$

By combining Eqn. (9) and (10) the nominal flux in the $\bar{X}_2$-direction can be written as

$$J_2 = -M_{22} \frac{\partial \mu}{\partial \bar{X}_2} = -\frac{D}{v}\left(\frac{\lambda_0}{\lambda} - \frac{1}{\lambda^2 \lambda_0^2}\right) \frac{\partial \bar{\mu}}{\partial \bar{X}_2} \tag{12}$$

where we can express $\frac{\partial \bar{\mu}}{\partial \bar{X}_2}$ through Eqn. (8) and use of the

chain rule

$$\frac{\partial \bar{\mu}}{\partial \bar{X}_2} = \frac{\partial}{\partial \bar{X}_2}\left(\frac{Nv\lambda}{\lambda_0} + \ln\frac{J-1}{J} + \frac{1-Nv}{J} + \frac{\chi}{J^2}\right) = \left(\frac{Nv}{\lambda_0} + \frac{1}{\left(\lambda_0^3\lambda - 1\right)\lambda} + \frac{Nv-1}{\lambda_0^3\lambda^2} - \frac{2\chi}{\lambda_0^6\lambda^3}\right)\frac{\partial \lambda}{\partial \bar{X}_2} \tag{13}$$

The conservation of solvent molecules requires

$$\frac{\partial C}{\partial t} = -\frac{\partial J_2\left(\bar{X}_2, t\right)}{\partial \bar{X}_2} \tag{14}$$

where $\frac{\partial C}{\partial t}$ can be obtained using Eqn. (11)

$$\frac{\partial C}{\partial t} = \frac{\lambda_0^3}{v}\frac{\partial \lambda}{\partial t} \tag{15}$$

Finally, by inserting Eqn. (13) into (12) we can write Eqn. (14) as

$$\frac{\partial \lambda}{\partial t} = \frac{D}{\lambda_0^3}\frac{\partial}{\partial \bar{X}_2}\left(\left(\frac{\lambda_0}{\lambda} - \frac{1}{\lambda^2\lambda_0^2}\right)\left(\frac{Nv}{\lambda_0} + \frac{1}{\left(\lambda_0^3\lambda - 1\right)\lambda} + \frac{Nv-1}{\lambda_0^3\lambda^2} - \frac{2\chi}{\lambda_0^6\lambda^3}\right)\frac{\partial \lambda}{\partial \bar{X}_2}\right) \tag{16}$$

Solving Eqn. (16), we obtain the stretch λ as a function of the coordinate $\bar{X}_2$ and time t. The corresponding chemical potential $\bar{\mu}\left(\bar{X}_2, t\right)$ can be found through the relation in Eqn. (8). We emphasize that the material properties of the gel will impact the chemical potential profile through the thickness, hence, a unique chemical profile must be calculated for each set of gel parameters.

3.3 Perturbation analysis

Based on the works by Kang and Huang [22] and Wu *et al.* [25, 27] we outline an eigenvalue problem that can be solved using a finite difference method. We introduce a small 2D perturbation from the swollen state given by the displacements u_1 and u_2 (illustrated with the dotted line shown in Fig. 1b). The deformation gradient tensor of the perturbed state $\tilde{\mathbf{F}}$ can be written as

$$\tilde{\mathbf{F}} = \begin{bmatrix} 1 + \frac{\partial u_1}{\partial x_1} & \lambda\frac{\partial u_1}{\partial x_2} & 0 \\ \frac{\partial u_2}{\partial x_1} & \lambda\left(1 + \frac{\partial u_2}{\partial x_2}\right) & 0 \\ 0 & 0 & 1 \end{bmatrix} \tag{17}$$

Retaining only linear terms of the perturbation, the volume ratio of the perturbed state is approximated by

$$\tilde{J} = \det\tilde{\mathbf{F}} \approx \lambda\left(1 + \frac{\partial u_1}{\partial x_1} + \frac{\partial u_2}{\partial x_2}\right) \tag{18}$$

Using the relation in Eqn. (8) to eliminate $\bar{\mu}$ in Eqn. (6) and again neglecting higher-order terms in the perturbation, the four in-plane nominal stress components of the perturbed state can be approximated by

$$s_{11} \approx NkT\left[\left(1+\lambda\xi\right)\frac{\partial u_1}{\partial x_1} + \lambda\left(\xi - \lambda\right)\frac{\partial u_2}{\partial x_2} - \lambda^2 + 1\right] \tag{19}$$

$$s_{22} \approx NkT\left[\left(\xi - \lambda\right)\frac{\partial u_1}{\partial x_1} + \left(\xi + \lambda\right)\frac{\partial u_2}{\partial x_2}\right] \tag{20}$$

$$s_{12} \approx NkT\lambda\left(\frac{\partial u_1}{\partial x_2} + \frac{\partial u_2}{\partial x_1}\right) \tag{21}$$

$$s_{21} \approx NkT\left(\lambda^2\frac{\partial u_1}{\partial x_2} + \frac{\partial u_2}{\partial x_1}\right) \tag{22}$$

where $\xi = \frac{1}{\lambda} + \frac{1}{Nv}\left(\frac{1}{\lambda - 1} - \frac{1}{\lambda} - \frac{2\chi}{\lambda^2}\right)$. In the absence of body forces, mechanical static equilibrium requires

$$\frac{\partial s_{11}}{\partial x_1} + \lambda\frac{\partial s_{12}}{\partial x_2} = 0 \tag{23}$$

$$\frac{\partial s_{21}}{\partial x_1} + \lambda\frac{\partial s_{22}}{\partial x_2} = 0 \tag{24}$$

Combining the perturbed stress components (eqs (19)-(22)) and the equilibrium equations (eqs (23) and (24)) gives two coupled differential equations

$$\left(1+\lambda\xi\right)\frac{\partial^2 u_1}{\partial x_1^2} + \lambda^2\frac{\partial^2 u_1}{\partial x_2^2} + \lambda\xi\frac{\partial^2 u_2}{\partial x_1 \partial x_2} + f_1\left(x_2\right)\left(\frac{\partial u_1}{\partial x_2} + \frac{\partial u_2}{\partial x_1}\right) = 0 \tag{25}$$

$$\frac{\partial^2 u_2}{\partial x_1^2} + \lambda\left(\xi + \lambda\right)\frac{\partial^2 u_2}{\partial x_2^2} + \lambda\xi\frac{\partial^2 u_1}{\partial x_1 \partial x_2} + f_2\left(x_2\right)\frac{\partial u_1}{\partial x_1} + f_3\left(x_2\right)\frac{\partial u_2}{\partial x_2} = 0 \tag{26}$$

where $f_1\left(x_2\right) = \frac{\lambda}{Nv}\frac{d}{dx_2}\left(\lambda Nv\right)$, $f_2\left(x_2\right) = \frac{\lambda}{Nv}\frac{d}{dx_2}\left[Nv\left(\xi - \lambda\right)\right]$, and $f_3\left(\bar{X}_2\right) = \frac{\lambda}{Nv}\frac{d}{dx_2}\left[Nv\left(\xi + \lambda\right)\right]$. We now assume the two perturbations to be harmonic

$$u_1 = U_1(x_2)\sin\omega x_1 \quad \text{and} \quad u_2 = U_2(x_2)\cos\omega x_1 \tag{27}$$

where ω is the wavenumber of the perturbations, and we can write the two equilibrium equations (eqs (25) and (26)) as

$$\begin{aligned}\lambda^2\frac{d^2U_1}{dx_2^2}+f_1\frac{dU_1}{dx_2}-\omega^2\left(1+\lambda\xi\right)U_1\\ -\omega\lambda\xi\frac{dU_2}{dx_2}-\omega f_1U_2=0\end{aligned} \tag{28}$$

$$\begin{aligned}\omega\lambda\xi\frac{dU_1}{dx_2}+\omega f_2U_1+\lambda\left(\xi+\lambda\right)\frac{d^2U_2}{dx_2^2}\\ +f_3\frac{dU_2}{dx_2}-\omega^2U_2=0\end{aligned} \tag{29}$$

As the material parameters of the gel are given in the reference coordinate system, we re-write the equilibrium equations in terms of $\bar{X}_2$, noting that x_2=$\lambda X_2 = H\lambda\bar{X}_2$ giving

$$\frac{d}{dx_2}=\frac{1}{H\lambda}\frac{d}{d\bar{X}_2} \tag{30}$$

and

$$\frac{d^2}{dx_2^2}=\frac{1}{H^2\lambda^2}\frac{d^2}{d\bar{X}_2^2}-\frac{1}{H^2\lambda^3}\frac{d\lambda}{d\bar{X}_2}\frac{d}{d\bar{X}_2} \tag{31}$$

The final equilibrium equations can then be written as

$$\begin{aligned}&\frac{d^2U_1}{d\bar{X}_2^2}+\lambda^{-2}\left[f_1\left(\bar{X}_2\right)-\lambda\frac{d\lambda}{d\bar{X}_2}\right]\frac{dU_1}{d\bar{X}_2}-\omega^2H^2\left(1+\lambda\xi\right)U_1\\ &-\omega H\xi\frac{dU_2}{d\bar{X}_2}-\omega H\lambda^{-1}f_1\left(\bar{X}_2\right)U_2=0\end{aligned} \tag{32}$$

$$\begin{aligned}&\omega H\xi\frac{dU_1}{d\bar{X}_2}+\omega H\lambda^{-1}f_2\left(\bar{X}_2\right)U_1+\lambda^{-1}\left(\xi+\lambda\right)\frac{d^2U_2}{d\bar{X}_2^2}+\\ &\lambda^{-2}\left[f_3\left(\bar{X}_2\right)-\left(\xi+\lambda\right)\frac{d\lambda}{d\bar{X}_2}\right]\frac{dU_2}{d\bar{X}_2}-\omega^2H^2U_2=0\end{aligned} \tag{33}$$

where $f_1\left(\bar{X}_2\right)=\frac{\lambda}{Nv}\frac{d}{d\bar{X}_2}\left(\lambda Nv\right)$, $f_2\left(\bar{X}_2\right)=\frac{\lambda}{Nv}\frac{d}{d\bar{X}_2}\left[Nv\left(\xi-\lambda\right)\right]$, and $f_3\left(\bar{X}_2\right)=\frac{\lambda}{Nv}\frac{d}{d\bar{X}_2}\left[Nv\left(\xi+\lambda\right)\right]$. We note that ωH can be considered a dimensionless wavenumber.

To complete the eigenvalue problem, we must include the boundary conditions at the lower and upper surface. The lower surface of the gel is attached to a rigid substrate giving

$$U_1\left(\bar{X}_2=0\right)=U_2\left(\bar{X}_2=0\right)=0 \tag{34}$$

The upper surface is traction free which implies that the out-of-plane stress components must be zero

$$s_{22}\left(\bar{X}_2=1\right)=s_{12}\left(\bar{X}_2=1\right)=0 \tag{35}$$

which by Eqn. (20) and (21) gives

$$\begin{aligned}&\left(\xi-\lambda\right)\frac{\partial u_1}{\partial x_1}+\left(\xi+\lambda\right)\frac{\partial u_2}{\partial x_2}=\\ &\omega H\lambda\frac{\xi-\lambda}{\xi+\lambda}U_1+\frac{\partial U_2}{\partial\bar{X}_2}=0,\ \text{for}\ \bar{X}_2=1\end{aligned} \tag{36}$$

and

$$\frac{\partial u_1}{\partial x_2}+\frac{\partial u_2}{\partial x_1}=\frac{\partial U_1}{\partial\bar{X}_2}-\omega H\lambda U_2=0,\ \text{for}\ \bar{X}_2=1 \tag{37}$$

3.4 Finite difference discretization

To solve the eigenvalue problem outlined in Section 3.3 while accounting for spatial variations in both material properties and chemical potential, we make use of the finite difference method. In contrast to Wu *et al.* [27], we formulate the equations for grids with non-uniform node spacing to improve computational efficiency. The grid consists of m nodes, numbered from 1 at the fixed bottom surface to m at the top free surface (see Fig. 1a). The central difference formulae for the first and second derivative of U_k^i (where i denotes the node number, k=1,2) can then be written as

$$\frac{dU_k^i}{d\bar{X}_2}\approx\alpha_1^iU_k^{i-1}+\beta_1^iU_k^i+\gamma_1^iU_k^{i+1} \tag{38}$$

$$\frac{d^2U_k^i}{d\bar{X}_2^2}\approx\alpha_2^iU_k^{i-1}+\beta_2^iU_k^i+\gamma_2^iU_k^{i+1} \tag{39}$$

By further defining $\bar{X}_2^i$ as the coordinate of node i and introducing $\Delta^i=\bar{X}_2^{i+1}-\bar{X}_2^i$ as the node spacing (see Fig. 1a), it can be shown that the best set of parameters (α, β, and γ) is [37]

$$\begin{aligned}\alpha_1^i&=-\frac{\Delta^i}{\Delta^{i-1}\left(\Delta^{i-1}+\Delta^i\right)}\\ \gamma_1^i&=\frac{\Delta^{i-1}}{\Delta^i\left(\Delta^{i-1}+\Delta^i\right)}\\ \beta_1^i&=-\alpha_1^i-\gamma_1^i\end{aligned} \tag{40}$$

$$\begin{aligned}\alpha_2^i&=\frac{2}{\Delta^{i-1}\left(\Delta^{i-1}+\Delta^i\right)}\\ \gamma_2^i&=\frac{2}{\Delta^i\left(\Delta^{i-1}+\Delta^i\right)}\\ \beta_2^i&=-\alpha_2^i-\gamma_2^i\end{aligned} \tag{41}$$

It can be noted that this approach gives a second-order accuracy of the first derivative, while the second-order

derivative in the general case is first-order accurate. However, if $\Delta^{i-1} = \Delta^i$, meaning we have a uniform node spacing, the coefficients in Eqn. (41) would give second-order accuracy. Hence, the accuracy obtained with non-uniformly spaced grids depends on the ratio between Δ^{i-1} and Δ^i, with improved accuracy for ratios close to unity.

By use of the central difference formulae to node i we can write the normalized equilibrium Eqn. (32) and (33) in the format

$$\begin{aligned} &A_1^i U_1^{i-1} + A_2^i U_2^{i-1} + A_3^i U_1^i \\ &+ A_4^i U_2^i + A_5^i U_1^{i+1} + A_6^i U_2^{i+1} = 0 \end{aligned} \tag{42}$$

$$\begin{aligned} &B_1^i U_1^{i-1} + B_2^i U_2^{i-1} + B_3^i U_1^i \\ &+ B_4^i U_2^i + B_5^i U_1^{i+1} + B_6^i U_2^{i+1} = 0 \end{aligned} \tag{43}$$

From the boundary condition in Eqn. (34) we have

$$U_1^1 = U_2^1 = 0 \tag{44}$$

For $i = 2,3,4,...,m$ we can find

$$\begin{aligned} A_1^i &= \alpha_2^i + \frac{\alpha_1^i}{(\lambda^i)^2}\left[f_1(\bar{X}_2) - \lambda^i \frac{d\lambda^i}{d\bar{X}_2}\right] \\ A_2^i &= -\alpha_1^i \omega H \xi^i \\ A_3^i &= \beta_2^i + \frac{\beta_1^i}{(\lambda^i)^2}\left[f_1(\bar{X}_2) - \lambda^i \frac{d\lambda^i}{d\bar{X}_2}\right] - \omega^2 H^2\left(1 + \lambda^i \xi^i\right) \\ A_4^i &= -\beta_1^i \omega H \xi^i - \frac{\omega H}{\lambda^i} f_1(\bar{X}_2) \\ A_5^i &= \gamma_2^i + \frac{\gamma_1^i}{(\lambda^i)^2}\left[f_1(\bar{X}_2) - \lambda^i \frac{d\lambda^i}{d\bar{X}_2}\right] \\ A_6^i &= -\gamma_1^i \omega H \xi^i \end{aligned} \tag{45}$$

and

$$\begin{aligned} B_1^i &= \alpha_1^i \omega H \xi^i \\ B_2^i &= \frac{\alpha_2^i}{\lambda^i}\left(\xi^i + \lambda^i\right) + \frac{\alpha_1^i}{(\lambda^i)^2}\left[f_3(\bar{X}_2) - \left(\xi^i + \lambda^i\right)\frac{d\lambda^i}{d\bar{X}_2}\right] \\ B_3^i &= \beta_1^i \omega H \xi^i + \frac{\omega H}{\lambda^i} f_2(\bar{X}_2) \\ B_4^i &= \frac{\beta_2^i}{\lambda^i}\left(\xi^i + \lambda^i\right) + \frac{\beta_1^i}{(\lambda^i)^2}\left[f_3(\bar{X}_2) - \left(\xi^i + \lambda^i\right)\frac{d\lambda^i}{d\bar{X}_2}\right] - \omega^2 H^2 \\ B_5^i &= \gamma_1^i \omega H \xi^i \\ B_6^i &= \gamma_2^i \frac{1}{\lambda^i}\left(\xi^i + \lambda^i\right) + \frac{\gamma_1^i}{(\lambda^i)^2}\left[f_3(\bar{X}_2) - \left(\xi^i + \lambda^i\right)\frac{d\lambda^i}{d\bar{X}_2}\right] \end{aligned} \tag{46}$$

For the uppermost node $i = m$, the amplitudes at the ghost node U_k^{m+1}, $k = 1,2$, must be solved for. Hence, we set the distance between the surface and the ghost node to $\Delta^m = \Delta^{m-1}$, and use central differences around the boundary condition in Eqn. (36) and (37)

$$U_1^{m+1} = U_1^{m-1} + C_1 U_2^m \tag{47}$$

$$U_2^{m+1} = U_2^{m-1} + C_2 U_1^m \tag{48}$$

where $C_1 = \frac{2}{\Delta^{m-1}}\omega\lambda^m$ and $C_2 = -\frac{2}{\Delta^{m-1}}\omega\lambda^m \frac{\xi^m - \lambda^m}{\xi^m + \lambda^m}$. The two discretized equations for the top surface node can then be rewritten as

$$\begin{aligned} &\left(A_1^m + A_5^m\right) U_1^{m-1} + \left(A_2^m + A_6^m\right) U_2^{m-1} \\ &+ \left(A_3^m + A_6^m C_2\right) U_1^m + \left(A_4^m + A_5^m C_1\right) U_2^m = 0 \end{aligned} \tag{49}$$

$$\begin{aligned} &\left(B_1^m + B_5^m\right) U_1^{m-1} + \left(B_2^m + B_6^m\right) U_2^{m-1} \\ &+ \left(B_3^m + B_6^m C_2\right) U_1^m + \left(B_4^m + B_5^m C_1\right) U_2^m = 0 \end{aligned} \tag{50}$$

Equations (42) and (43) can be organized as

$$\mathbf{KU} = \mathbf{0} \tag{51}$$

where the matrix $\mathbf{K}(\omega H, Nv(\bar{X}_2), \chi(\bar{X}_2), \lambda(\bar{X}_2, t))$ have the dimensions $(2(m-1) \times 2(m-1))$ and consists of the coefficients A and B for each node while the vector $\mathbf{U}$ is organized as $\mathbf{U} = \left[U_1^2, U_2^2, ..., U_1^m, U_2^m\right]^T$. The stability of the gel is governed by the determinant of the matrix $\mathbf{K}$ and instability will occur when

$$\det \mathbf{K} = 0 \tag{52}$$

We note that the eigenvalue problem outlined in this section needs the stretch in each node λ^i as input. This stretch value is calculated using Eqn. (8) with the material properties and the chemical potential obtained in Section 3.2 as input.

3.5 Spatial discretization

For $\bar{t}_r = 0$, the chemical potential profile will display sharp gradients close to the upper surface of the gel at the beginning of the swelling process. This means that a short inter-node distance is needed in this region to obtain converged results. Close to the lower surface, on the other hand, there are small gradients, and a larger node spacing can be used. Hence, to improve the computational efficiency, the node spacing can be gradually increased towards the bottom

of the gel without significant loss of accuracy (see the convergence study in the supplemental material). We assign the uppermost node spacing Δ^{m-1} and calculate the following inter-node distances by the algorithm

$$\Delta^i = \begin{cases} \Delta^{m-1} & \text{if } \bar{X}_2 \geq (1-\rho) \\ \Delta^{i+1}(1+\alpha) & \text{if } \bar{X}_2 < (1-\rho) \end{cases} \tag{53}$$

working from $i = m-2$ to $i = 1$. The parameter ρ is a user input that defines a fraction of the gel with uniform node spacing. It can be noted that $\alpha = 0$ gives a uniform grid throughout the gel. To ease the comparison between uniform and non-uniform grids we introduce $m^* = \left(1/\Delta^{m-1}\right) + 1$, being a measure of the inter-node distance close to the upper surface. For the case of a uniformly spaced grid, m^* would equal the number of nodes in the grid (i.e. $m^* = m$ for $\alpha = 0$). Further, two grids with the same m^* value will have the same node spacing in the uniform part of the grid, although the total number of nodes m might differ.

3.6 Implementation

The framework outlined in the previous sections has been implemented in Python and the code is made freely available [29]. The stability criterion in Eqn. (52) is solved using a bisection method in SciPy, searching for a critical time step $t_c > 0$ where the chemical profile $\bar{\mu}(\bar{X}_2, t_c)$ causes instability. This search is performed for a discrete set of the dimensionless wavenumber ωH for each set of material parameters $Nv(\bar{X}_2)$ and $\chi(\bar{X}_2)$. The critical global out-of-plane stretch λ_c apparent at the onset of instability is approximated from the local stretch in each node λ_c^i through

$$\lambda_c = \frac{h}{H} \approx \sum_{i=1}^{m} \frac{\Delta^i + \Delta^{i-1}}{2} \lambda_c^i \tag{54}$$

where $\Delta^i = \bar{X}_2^{i+1} - \bar{X}_2^i$ is a dimensionless number and $\Delta^0 = \Delta^m = 0$.

So, one critical stretch value can be found for each discrete value of the dimensionless wavenumber. As the global stretch of the gel is increasing monotonically during the swelling process, the smallest critical stretch value yields the state of the gel at the onset of instability. Hence, the global out-of-plane stretch of a gel at instability λ_i is found from

$$\lambda_i = \min(\lambda_c) \tag{55}$$

A computational pipeline for the implementation can be found in the supplemental material.

3.7 Convergence

A vital feature of a computational framework as described here is the convergence of the method for a refinement of the discretization. The proposed procedure was found to yield converged results for the mesh parameters $m^* = 5000$, $\alpha = 0.01$ and $\rho = 0.12$ for $\bar{t}_r = \infty$, and $m^* = 40000$, $\alpha = 0.01$ and $\rho = 0.12$ for calculations with $\bar{t}_r = 0$. Hence, these mesh parameters are used for all presented results.

A detailed discussion on the convergence of the code can be found in the supplemental material.

4 Results and discussion

4.1 Preliminaries

Due to the availability of benchmark results, we choose to demonstrate the framework outlined in Section 3 for bilayered plates. In such plates, the cross-linking density through the thickness is given as

$$N(\bar{X}_2) = \begin{cases} N_b & \text{if } \bar{X}_2 < (1-\eta) \\ N_t & \text{if } \bar{X}_2 \geq (1-\eta) \end{cases} \tag{56}$$

where N_t and N_b are the cross-linking densities in the top and bottom layers of the gel respectively. The parameter η represents the thickness of the top layer as a fraction of the total gel thickness and is the following set to 0.1. We introduce the stiffness ratio as

$$n = N_t / N_b \tag{57}$$

and limit the scope of this study to $1 < n \leq 20$, giving hard-on-soft configurations in the low to moderate stiffness ratio range. The parameter χ is assumed constant through the plate.

We study the stability of gels for the two limiting cases of the normalized ramping time of the boundary condition, $\bar{t}_r = \infty$ and $\bar{t}_r = 0$. For the latter case, the profile of the chemical potential through the thickness of the gel is calculated for the given set of material parameters by solving Eqn. (16) with respect to time and calculating the corresponding chemical potential profiles before the perturbation analysis is performed. For the presentation of the results, we introduce the normalized wavelength of the perturbation

$$\bar{\Lambda} = \Lambda / H \tag{58}$$

where $\Lambda = 2\pi/\omega$ is the wavelength in dimensional units.

4.2 Effect of swelling kinetics

4.2.1 $\bar{t}_r = \infty$ vs $\bar{t}_r = 0$

To highlight the effect the swelling kinetics has on the state of the gel at the onset of instability, Fig. 3a shows the resulting stability plots for $\bar{t}_r = \infty$ and $\bar{t}_r = 0$ with the material parameters $N_b v = 0.01$, $n = 2$, and $\chi = 0.5$. The markers in the plot indicate the swelling ratio and normalized wavelength where instability of the gel would initiate (i.e. λ_i and $\bar{\Lambda}_i$). The plot demonstrates that the kinetics

of the swelling process can play an important role for the stability diagrams of the gels with instability occurring at a significantly lower swelling ratio and wavelength for $\bar{t}_r = 0$ compared with $\bar{t}_r = \infty$.

To showcase the significance of the upper and lower limit solution provided by the PA approach, λ_i from $\bar{t}_r = \infty$ and $\bar{t}_r = 0$ are compared with the FE results from Ilseng *et al.* [21] in Fig. 3b. This illustrates how the upper and lower bound PA results represent the plateau levels obtained for large and small values of $\bar{t}_r$ in the FE simulations. It should be noted that the range in the normalized ramping time where the transition between the two plateau levels happens depends on the stiffness properties of the gel, as discussed in [21].

For low values of $\bar{t}_r$, the FE simulations can be seen to predict a slightly lower λ_i than the PA method. This discrepancy between the methods could stem from the fact that the PA method calculates the point of onset of instability directly, while in the FEM approach the onset of instability is estimated based on the topology of the gel surface [21].

4.2.2 Effect of stiffness ratio

To illustrate how the effect of the swelling kinetics depends on the stiffness ratio of a bilayered gel, Fig. 4 presents (a) the swelling ratio at instability, (b) the normalized wavelength at instability, and (c) the dimensionless time to instability for stiffness ratios between 1.5 and 20.

The stability plot shown in Fig. 4a illustrates how the swelling ratio at instability drops for increasing stiffness ratios for both the limiting cases, $\bar{t}_r = \infty$ and $\bar{t}_r = 0$. The shaded area between the two curves indicates the range in which instability can occur for a gel with a specific stiffness ratio, depending on the timescale of the diffusion process (i.e. the value of $\bar{t}_r$). For a fast diffusion process, instability will occur close to the blue solid line, while a slow diffusion process would lead to instability close to the dashed red line. From the plot, it can be concluded that the effect of the swelling kinetics for the swelling ratio at instability is reduced with larger stiffness ratios. The results obtained with the presented method are also compared with FE results from [21] for $\bar{t}_r = 10^{-4}$ and $\bar{t}_r = 10^6$ at n values of 2, 5, and 20. The two methods shows a good correspondence, although the PA results for $\bar{t}_r = 0$ are slightly above the FE results for $\bar{t}_r = 10^{-4}$, as already discussed for $n = 2$ in Section 4.2.1.

The change in the normalized wavelength at instability with a change in stiffness ratio is shown in Fig. 4b. We see a clear trend of increasing wavelength for increasing stiffness ratio for the case of $\bar{t}_r = 0$. For $\bar{t}_r = \infty$, on the other hand, the wavelength first decreases as the stiffness ratio goes from 1.5 to 3, before it increases as the stiffness ratio is increased further. The slightly irregular trend of the two curves are caused by numerical artefacts as instability is checked at discrete values of ωH. Further, FEM results based on previous simulations [21] are shown for n values of 2, 5, and 20. While both PA and FEM disclose the same trend of a generally increasing normalized wavelength for increased stiffness ratios, it can be observed that FEM simulations predicts a lower normalized wavelength at instability compared to the PA results. There can be multiple sources for this discrepancy. I) The PA method assumes an infinite plate, while a finite width is used in the FEM simulations. II) In the PA method, the wavelength at instability is calculated directly, while in the FEM approach the wavelength is estimated from the instability pattern occurring in the model. III) As the stability diagram in the ($\bar{\Lambda}$,λ_c)-plane often shows a low critical swelling ratio for a wide range of wavelengths (see as an example Fig. 5a, n=20), small numerical variations can lead to significant changes in the predicted wavelength at instability for both the FEM and the PA approach. However, this sensitivity is expected to be reflected in experiments as a high variability in the measured critical wavelength due to variations in experimental imperfections.

The dimensionless time to instability is shown in Fig. 4c. The time to instability t_c is normalized by the time of the ramping process t_r for the $\bar{t}_r = \infty$ results (solid blue line) referring to the left ordinate. Through this normalization, the critical time to instability can be interpreted as the increase in the chemical potential in the gel relative to the maximum increase. This means that $t_c/t_r \leq 1$, where $t_c/t_r = 1$ represents the case where the onset of instability happens when the gel reaches a homogeneous normalized chemical potential of $\bar{\mu}_1$. The time to instability results for $\bar{t}_r = 0$ (dashed red line) are normalized by τ and corresponds to the right ordinate. From the plot it is clear that the critical time to instability drops gradually with increased stiffness for homogeneous swelling, i.e. $\bar{t}_r = \infty$. For the $\bar{t}_r = 0$ results, on the other hand, the critical time to instability drops significantly as the stiffness ratio increase from 1.5 to 5. For stiffness ratios larger than 5, instability happens almost immediately after the surface is exposed to an increased chemical potential. The latter fact correlates to the small swelling ratio at instability, observed in Fig. 4a.

4.2.3 Change of instability mode for soft gels

Studies assuming homogeneous chemical potentials in bilayered gels have found that long-wavelength instability modes occur for hard-on-soft configurations, while instability in the short-wavelength limit would be obtained for soft-on-hard configurations [25, 27]. However, studies assessing transient swelling states through the use of FE simulations have found that bilayered gels with a sufficiently soft substrate combined with a low stiffness ratio can display instabilities in the short-wavelength limit even for hard-on-soft configurations [20, 21]. Such short-wavelength instability modes are known to be highly unstable and to easily collapse to creases [38].

Using the proposed PA method, this change of mode with a change in the swelling kinetics is illustrated in Fig. 5, showing the stability curves for $N_b v = 10^{-3}$ and three different values of the stiffness ratio n for $\bar{t}_r = \infty$ (Fig. 5a) and $\bar{t}_r = 0$ (Fig. 5b). For $\bar{t}_r = \infty$, we see that a long-wavelength instability mode is predicted for all values of n. For $\bar{t}_r = 0$, on the other hand, we see a competition between short-wavelength and long-wavelength instability modes for

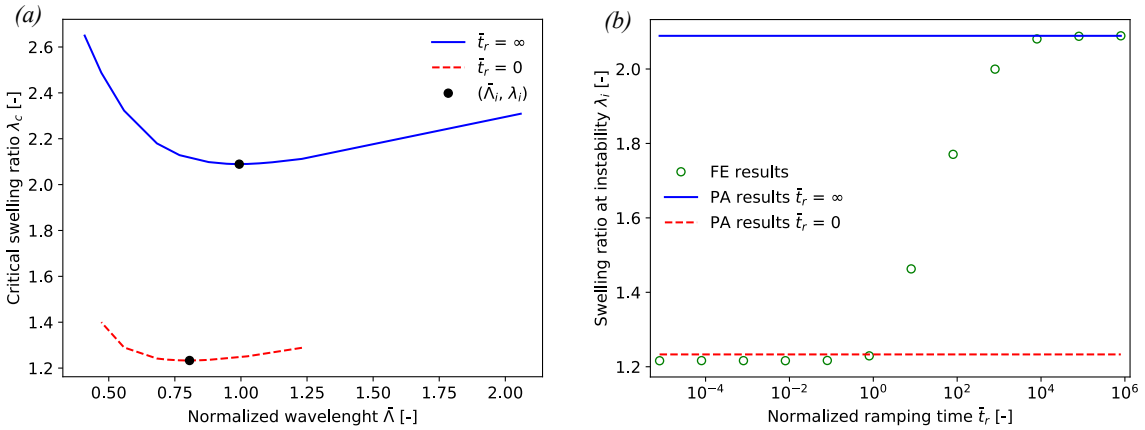

Fig. 3: *(a)* Comparison of stability curves for infinite and zero normalized ramping times and *(b)* evolution of λ_i from $\bar{t}_r \approx 0$ to $\bar{t}_r \approx \infty$ obtained with FE simulations and compared with the PA results. The material parameters $N_b v = 0.01$, $n = 2$, and $\chi = 0.5$ were used.

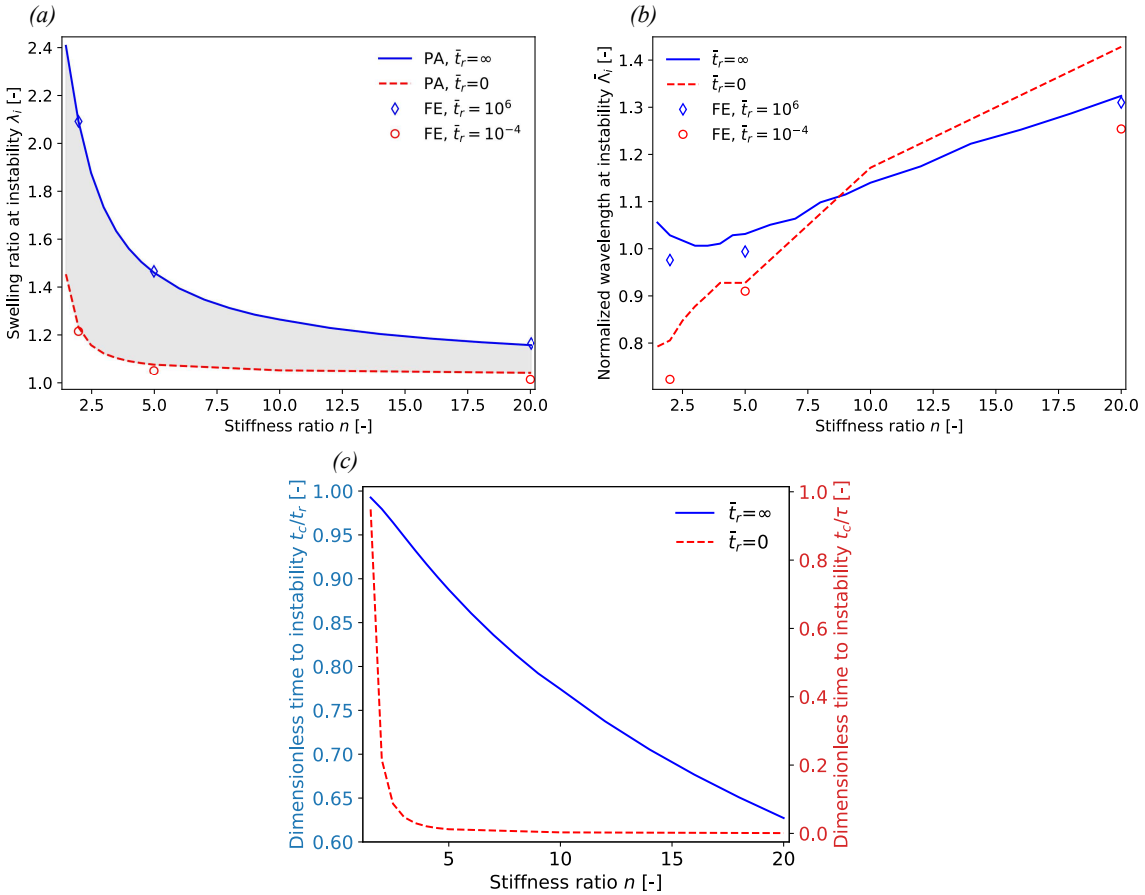

Fig. 4: *(a)* Critical swelling ratio, *(b)* normalized critical wavelength, and *(c)* dimensionless time to onset of instability ($\bar{t}_r = \infty$ results refers to left ordinate and $\bar{t}_r = 0$ results refers to right ordinate). The shaded area in *(a)* indicates the instability swelling ratio that can be obtained for a given value of n depending on the normalized ramping time. The markers in *(a)* and *(b)* indicate results obtained using finite element simulations [21]. The parameters $N_b v = 0.01$ and $\chi = 0.5$ are used.

the gels with a low stiffness ratio. Specifically, for a stiffness ratio of $n = 2$, the global minimum state tends towards the short-wavelength limit and a low critical swelling ratio. Still, a long-wavelength instability mode is found as a local minimum at a critical swelling ratio of 1.15. For $n = 5$, the global minimum state is found for a long-wavelength mode, however, the critical swelling ratio is rapidly decreasing towards the shorter wavelengths. Note that the accuracy of the presented model is compromised at extreme values of the dimensionless wavenumber ωH, hence, accurate stability pre-

dictions for very small values of $\bar{\Lambda} = 2\pi/\omega H$ are inaccessible. However, we assume that the trend in the curves for $n = 2$ and $n = 5$ would continue towards the shorter wavelengths, and that experimental realizations of these configurations would display immediate instability in the short-wavelength limit. For $n = 20$, on the other hand, the stiffness ratio is sufficiently high such that the global minimum is a long-wavelength mode and instability is not predicted for low values of $\bar{\Lambda}$ (note that the curve for $n = 20$ stops at $\bar{\Lambda} \approx 0.3$ as no instability point was found for $0.1 \leq \bar{\Lambda} \leq 0.3$). Regarding the spatial-temporal discretization of the problem, it can be noted that calculations with a refinement of the nodal distance (specifically $m^* = 80000$) replicate the results presented in Fig. 5b. Further, the initial time step t_1 is set sufficiently small ($t_1/\tau \approx 1 \cdot 10^{-4}$) such that the first occurrence of instability is found after multiple time steps. Hence, a further refinement of the temporal discretization of Eqn. (16) is not expected to impact the presented data.

The results in Fig. 5b illustrate the competition between short- and long-wavelength instability modes for soft gels with a low stiffness ratio, and are in line with our previous results obtained through FE simulations, finding a short-wavelength instability mode in combination with a low instability swelling ratio for $N_b v = 10^{-3}$ combined with $n = 2$ and $n = 5$, while a long-wavelength instability mode was obtained for $n = 20$ [21]. Further, these results highlight the importance of accounting for the transient nature of the swelling problem for predictions of both the critical swelling ratio and the instability mode.

5 Concluding remarks

We have presented a new approach for predicting upper and lower bounds for the stability of transiently swelling hydrogels using a linear perturbation analysis framework, and the implemented code is made freely available online [29]. The framework is demonstrated for a bilayered plate structure for which it shows a clear convergence for a refined discretization and good correspondence with previously published results.

Adding the transient effects provides a new lower bound to the degree of swelling at the onset of instability of bilayered plates, complementing previous upper bound results obtained through an assumption of a homogeneous chemical potential. The proposed method also sheds light on the competition between short- and long-wavelength instability modes for soft gels with a low stiffness ratio exposed to diffusive swelling.

Using the proposed model, it is straight forward to obtain results also for other variations of through-thickness plate stiffness, and in other ranges of chemical potentials. Further, the proposed computational method could be used to study the onset of instability for specific types of hydrogels, e.g. temperature-sensitive ones, or other geometries, e.g. spheres. However, changing the constitutive formulation or geometrical assumptions would require the derivation and implementation of a new model.

Compared with finite element simulations, the presented approach excels in simplicity, computational cost, and availability. We believe that the provided code can be used to obtain guidelines for experimental testing and new applications of graded hydrogels under diffusion induced swelling, providing estimates of the stability range for both fast and slow diffusion. The main disadvantage of the presented methodology is its limitation to simple geometries and loading conditions. For the ability to predict the stability range of general geometries and loading conditions, in addition to access to the post-buckling behavior, a finite element framework would be more suited.

Acknowledgements

This work was supported by the Research Council of Norway (Project no 240299/F20).

References

[1] Bysell, H., and Malmsten, M., 2006. "Visualizing the interaction between poly-L-lysine and poly(acrylic acid) microgels using microscopy techniques: Effect of electrostatics and peptide size". *Langmuir,* **22**, pp. 5476–5484.

[2] Culver, H. R., Clegg, J. R., and Peppas, N. A., 2017. "Analyte-Responsive Hydrogels: Intelligent Materials for Biosensing and Drug Delivery". *Accounts of Chemical Research,* **50**, pp. 170–178.

[3] Li, J., and Mooney, D. J., 2016. "Designing hydrogels for controlled drug delivery". *Nature Reviews Materials,* **1**, p. 16071.

[4] Buenger, D., Topuz, F., and Groll, J., 2012. "Hydrogels in sensing applications". *Progress in Polymer Science,* **37**, pp. 1678–1719.

[5] Tierney, S., Hjelme, D. R., and Stokke, B. T., 2008. "Determination of swelling of responsive gels with nanometer resolution. Fiber-optic based platform for hydrogels as signal transducers". *Analytical Chemistry,* **80**, pp. 5086–5093.

[6] Holmes, D. P., and Crosby, A. J., 2007. "Snapping surfaces". *Advanced Materials,* **19**, pp. 3589–3593.

[7] Tanaka, T., Sun, S. T., Hirokawa, Y., Katayama, S., Kucera, J., Hirose, Y., and Amiya, T., 1987. "Mechanical instability of gels at the phase transition". *Nature,* **325**, pp. 796–798.

[8] Breid, D., and Crosby, A. J., 2009. "Surface wrinkling behavior of finite circular plates". *Soft Matter,* **5**, pp. 425–431.

[9] Guvendiren, M., Yang, S., and Burdick, J. A., 2009. "Swelling-Induced surface patterns in hydrogels with gradient crosslinking density". *Advanced Functional Materials,* **19**, pp. 3038–3045.

[10] Dervaux, J., and Amar, M. B., 2012. "Mechanical Instabilities of Gels". *Annual Review of Condensed Matter Physics,* **3**, pp. 311–332.

[11] Bertrand, T., Peixinho, J., Mukhopadhyay, S., and MacMinn, C. W., 2016. "Dynamics of Swelling and

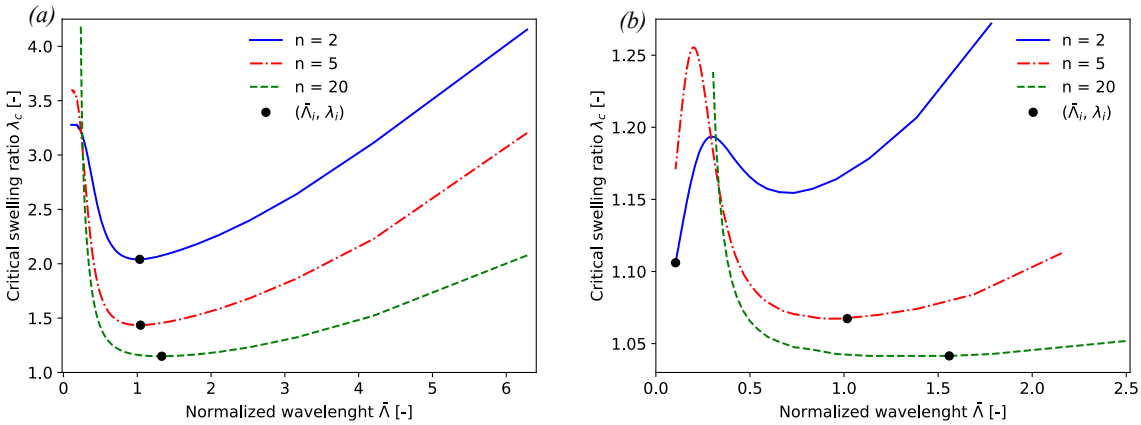

Fig. 5: Stability plots for *(a)* $\bar{t}_r = \infty$ and *(b)* $\bar{t}_r = 0$, using material parameters $N_b v = 0.001$ and $\chi = 0.5$.

Drying in a Spherical Gel". *Physical Review Applied,* **6**, pp. 1–20.

[12] Guvendiren, M., Burdick, J. A., and Yang, S., 2010. "Kinetic study of swelling-induced surface pattern formation and ordering in hydrogel films with depth-wise crosslinking gradient". *Soft Matter,* **6**, pp. 2044–2049.

[13] Sultan, E., and Boudaoud, A., 2008. "The Buckling of a Swollen Thin Gel Layer Bound to a Compliant Substrate". *Journal of Applied Mechanics,* **75**, pp. 51002–51005.

[14] Prot, V., Sveinsson, H. M., Gawel, K., Gao, M., Skallerud, B., and Stokke, B. T., 2013. "Swelling of a hemi-ellipsoidal ionic hydrogel for determination of material properties of deposited thin polymer films: an inverse finite element approach". *Soft Matter,* **9**, pp. 5815–5827.

[15] Tallinen, T., Chung, J. Y., Rousseau, F., Girard, N., Lefevre, J., and Mahadevan, L., 2016. "On the growth and form of cortical convolutions". *Nat Phys,* **12**, pp. 588–593.

[16] Weiss, F., Cai, S., Hu, Y., Kyoo Kang, M., Huang, R., and Suo, Z., 2013. "Creases and wrinkles on the surface of a swollen gel". *Journal of Applied Physics,* **114**, p. 073507.

[17] Bouklas, N., Landis, C. M., and Huang, R., 2015. "A nonlinear, transient finite element method for coupled solvent diffusion and large deformation of hydrogels". *Journal of the Mechanics and Physics of Solids,* **79**, pp. 21–43.

[18] Toh, W., Ding, Z., Yong Ng, T., and Liu, Z., 2015. "Wrinkling of a Polymeric Gel During Transient Swelling". *Journal of Applied Mechanics,* **82**, p. 061004.

[19] Yu, C., Malakpoor, K., and Huyghe, J. M., 2018. "A three-dimensional transient mixed hybrid finite element model for superabsorbent polymers with strain-dependent permeability". *Soft Matter,* **14**, pp. 3834–3848.

[20] Dortdivanlioglu, B., and Linder, C., 2019. "Diffusion-driven swelling-induced instabilities of hydrogels". *Journal of the Mechanics and Physics of Solids,* **125**, pp. 38–52.

[21] Ilseng, A., Prot, V., Skallerud, B. H., and Stokke, B. T., 2019. "Buckling initiation in layered hydrogels during transient swelling". *Journal of the Mechanics and Physics of Solids,* **128**, pp. 219–238.

[22] Kang, M. K., and Huang, R., 2010. "Swell-induced surface instability of confined hydrogel layers on substrates". *Journal of the Mechanics and Physics of Solids,* **58**, pp. 1582–1598.

[23] Kang, M. K., and Huang, R., 2010. "Effect of surface tension on swell-induced surface instability of substrate-confined hydrogel layers". *Soft Matter,* **6**, p. 5736.

[24] Xiao, Z., Li, M., and Zhou, J., 2012. "Surface instability of a swollen cylinder hydrogel". *Acta Mechanica Solida Sinica,* **25**, pp. 550–556.

[25] Wu, Z., Bouklas, N., and Huang, R., 2013. "Swell-induced surface instability of hydrogel layers with material properties varying in thickness direction". *International Journal of Solids and Structures,* **50**, pp. 578–587.

[26] Nardinocchi, P., and Puntel, E., 2017. "Swelling-induced wrinkling in layered gel beams". *Proceedings of the Royal Society A: Mathematical, Physical and Engineering Sciences,* **473**.

[27] Wu, Z., Bouklas, N., Liu, Y., and Huang, R., 2017. "Onset of swell-induced surface instability of hydrogel layers with depth-wise graded material properties". *Mechanics of Materials,* **105**, pp. 138–147.

[28] Biot, M. A., 1963. "Surface instability of rubber in compression". *Applied Scientific Research, Section A,* **12**, pp. 168–182.

[29] Ilseng, A., 2019. Ilseng/transient-gel-instability v1.0, doi: 10.5281/ZENODO.3578199.

[30] Caccavo, D., Cascone, S., Lamberti, G., and Barba, A. A., 2018. "Hydrogels: experimental characterization and mathematical modelling of their mechanical and diffusive behaviour". *Chem. Soc. Rev.,* **47**, pp. 2357–2373.

[31] Hong, W., Zhao, X., Zhou, J., and Suo, Z., 2008. "A theory of coupled diffusion and large deformation in

polymeric gels". *Journal of the Mechanics and Physics of Solids,* **56**, pp. 1779–1793.

[32] Hong, W., Liu, Z., and Suo, Z., 2009. "Inhomogeneous swelling of a gel in equilibrium with a solvent and mechanical load". *International Journal of Solids and Structures,* **46**, pp. 3282–3289.

[33] Flory, P. J., 1953. *Principles of polymer chemistry*. Cornell University Press.

[34] Huggins, M. L., 1941. "Solutions of Long Chain Compounds". *The Journal of Chemical Physics,* **9**, pp. 440–440.

[35] Flory, P. J., 1942. "Thermodynamics of High Polymer Solutions". *The Journal of Chemical Physics,* **10**, pp. 51–61.

[36] Bouklas, N., and Huang, R., 2012. "Swelling kinetics of polymer gels: comparison of linear and nonlinear theories". *Soft Matter,* **8**, p. 8194.

[37] Sfakianakis, N., 2009. "Finite difference schemes on non-uniform meshes for hyperbolic conservation laws". PhD thesis.

[38] Cao, Y., and Hutchinson, J. W., 2012. "From wrinkles to creases in elastomers: the instability and imperfection-sensitivity of wrinkling". *Proceedings of the Royal Society A: Mathematical, Physical and Engineering Sciences,* **468**, pp. 94–115.

Supplementary data to: "A Perturbation Analysis Approach for Studying the Effect of Swelling Kinetics on Instabilities in Hydrogel Plates"

The following provides the supplementary data to: Ilseng, A., Skallerud, B.H., Stokke, B.T., and Prot, V., 2021. "A Perturbation Analysis Approach for Studying the Effect of Swelling Kinetics on Instabilities in Hydrogel Plates" *Journal of Applied Mechanics*, **88**(5), doi: https://doi.org/10.1115/1.4049633. The document gives a description of the computational pipeline for the implementation of the method described in the paper and the convergence of the code.

1 Computational pipeline

An illustration of the computational pipeline used for the implementation of the presented framework is outlined in Algorithm 1.

Algorithm 1 Computational pipeline

Input: t, $Nv(\bar{X}_2)$, $\chi(\bar{X}_2)$, $\bar{t}_r$, $\omega Hlist$
if $\bar{t}_r = 0$ **then**
    Calculate $\bar{\mu}(\bar{X}_2, t)$ ▷ Equations (16) and (8)
else if $\bar{t}_r = \infty$ **then**
    Define a homogeneous $\bar{\mu}(t)$
end if
while $\omega Hlist$ is coarse **do**
    for `each` ωH `in` $\omega Hlist$ **do**
        Search for t_c such that $\det \mathbf{K}(\bar{\mu}(\bar{X}_2, t_c)) = 0$ ▷ Equation (52)
        Calculate $\lambda(\bar{X}_2, t_c)$ from $\bar{\mu}(\bar{X}_2, t_c)$ ▷ Equation (8)
        Calculate λ_c from $\lambda(\bar{X}_2, t_c)$ ▷ Equation (54)
        Add λ_c to $\lambda_c list$
    end for
    Refine $\omega Hlist$ around $\min(\lambda_c list)$
end while
Save $\lambda_c list$ and $\omega Hlist$ to file

2 Convergence

2.1 $\bar{t}_r = \infty$

For the case of a normalized ramping time $\bar{t}_r = \infty$ the gel will always be in chemical equilibrium with its surroundings. Hence, the gradient governing the precision of the finite difference discretization will be the stiffness distribution through the thickness, yielding a slower convergence for larger stiffness ratios. Therefore, the convergence is studied for a stiffness ratio of $n = 20$. In Supplemental Fig. 1, the stability curves obtained with various grids are compared with a direct bilayer method solving the eigenvalue problem without the use of a finite difference discretization [1]. The direct bilayer method is described by Wu *et al.* [1] and our implementation of this method in Python is available online [2]. It can be noted that the direct bilayer method is computationally very efficient, however, it is limited to bilayered configurations with homogeneous chemical potentials. Supplemental Fig. 1a presents the convergence for grids with uniform node spacing (i.e. $\alpha = 0$, $m = m^*$). We see that the finite difference discretization with 1000 uniformly spaced nodes predicts a too low critical swelling, especially for long and short wavelengths. Increasing to 5000 nodes through the plate, the finite difference approach yields good correspondence with the direct bilayer method, being able to reproduce the minimum point of the curve and only slightly underestimating the critical swelling ratio at very large wavelengths. We note that convergence for 5000 nodes in a uniform grid is in line with previous studies [3].

Supplemental Fig. 1b compares the stability curve from using 5000 evenly spaced nodes to that obtained using a non-uniform grid with the parameters $m^* = 5000$, $\alpha = 0.01$, and $\rho = 0.12$, giving a total of 983 nodes in the grid. Note that the two grids have the same node density in the upper 12 % of the gel and that $\rho > \eta$ such that the fine grid includes the layer interface. In the lower 88 % of the non-uniform grid, the node spacing increases by 1 % for each node. The resulting instability curves using the uniform and the non-uniform grids are indistinguishable. We note that increasing the number of nodes in the grid by a factor k was found to increase the computation time by a factor $k^{2.25}$. Hence, reducing the number of nodes from 5000 to 983 reduced the computation time from hours to a few minutes on a normal desktop computer.

2.2 $\bar{t}_r = 0$

For the case of a normalized ramping time $\bar{t}_r = 0$ the gradient of the chemical potential in the gel dominates the accuracy of the code and we find the slowest convergence for the lowest stiffness gradients. Hence, the convergence of the code is shown in Supplemental Fig. 2 for $n = 1.5$. Supplemental Fig. 2a compares the instability curves for four different non-uniform grids, while Supplemental Fig. 2b shows how the instability swelling ratio λ_i depends on the node den-

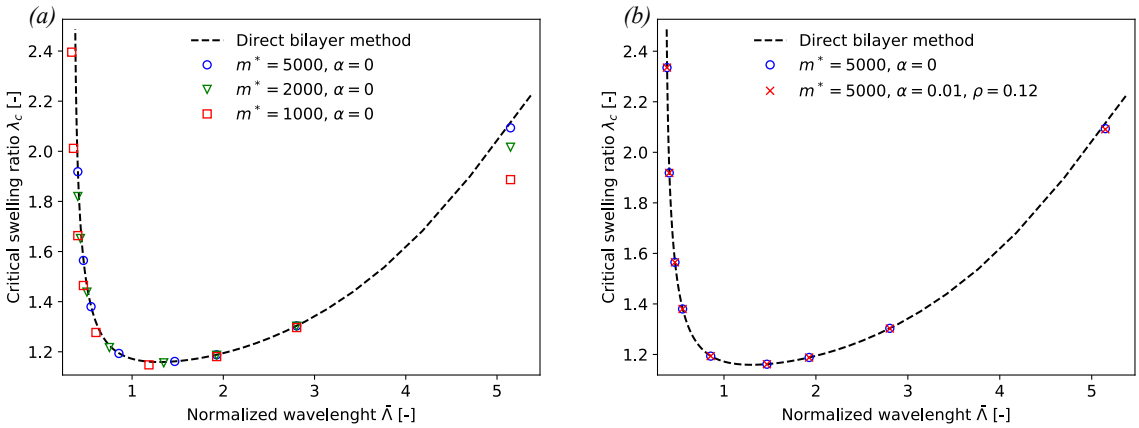

Supplemental Fig. 1: Convergence of the code for a bilayered gel with $\bar{t}_r = \infty$. (a) The stability plots for uniform grids compared with the direct bilayer solution. (b) A comparison of stability plots for uniform and non-uniform grids having the same value for m^*. The material parameters $N_b v = 0.01$, $n = 20$ and $\chi = 0.5$ were used.

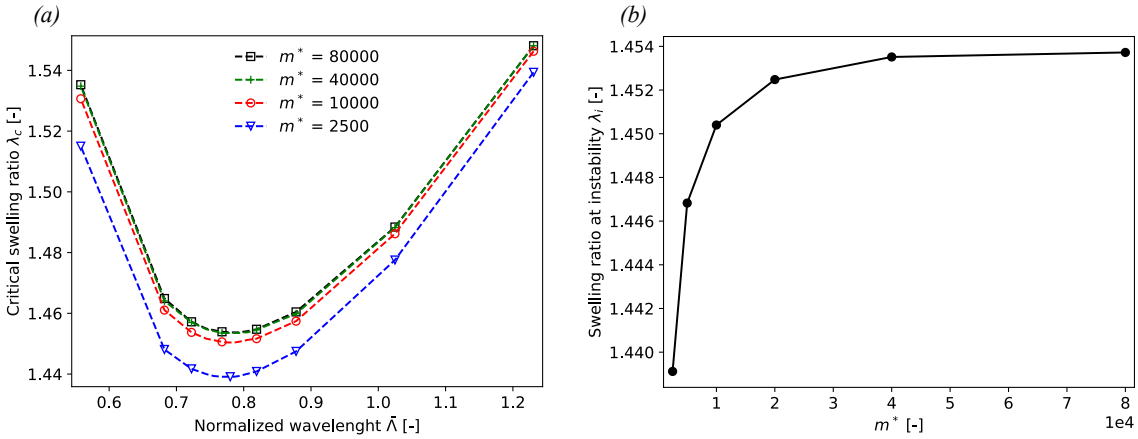

Supplemental Fig. 2: (a) Stability plots for a bilayered gel with $\bar{t}_r = 0$. (b) The convergence of the swelling ratio at the onset of instability λ_i for reduced node spacing in the upper part of the gel. The grid parameters $\alpha = 0.01$ and $\rho = 0.12$ and material parameters $N_b v = 0.01$, $n = 1.5$ and $\chi = 0.5$ were used.

sity towards the surface of the gel. From the two plots in Supplemental Fig. 2, it can be concluded that $m^* = 40000$ yields converged results for both the stability diagram and λ_i.

References

[1] Wu, Z., Bouklas, N., and Huang, R., 2013. "Swell-induced surface instability of hydrogel layers with material properties varying in thickness direction". *International Journal of Solids and Structures,* **50**, pp. 578–587.

[2] Ilseng, A., 2019. Ilseng/bilayer-instability v1.0, doi:10.5281/ZENODO.3550624.

[3] Wu, Z., Bouklas, N., Liu, Y., and Huang, R., 2017. "Onset of swell-induced surface instability of hydrogel layers with depth-wise graded material properties". *Mechanics of Materials,* **105**, pp. 138–147.